Scaling the Aspect Ratio of Nanoscale Closely Packed Silicon Vias by MacEtch: Kinetics of Carrier Generation and Mass Transport

*Jeong Dong Kim, Parsian K. Mohseni, Karthik Balasundaram, Srikanth Ranganathan, Jayavel Pachamuthu, James J. Coleman, and Xiuling Li**

Metal-assisted chemical etching (MacEtch) has shown tremendous success as an anisotropic wet etching method to produce ultrahigh aspect ratio semiconductor nanowire arrays, where a metal mesh pattern serves as the catalyst. However, producing vertical via arrays using MacEtch, which requires a pattern of discrete metal disks as the catalyst, has often been challenging because of the detouring of individual catalyst disks off the vertical path while descending, especially at submicron scales. Here, the realization of ordered, vertical, and high aspect ratio silicon via arrays by MacEtch is reported, with diameters scaled from 900 all the way down to sub-100 nm. Systematic variation of the diameter and pitch of the metal catalyst pattern and the etching solution composition allows the extraction of a physical model that, for the first time, clearly reveals the roles of the two fundamental kinetic mechanisms in MacEtch, carrier generation and mass transport. Ordered submicron diameter silicon via arrays with record aspect ratio are produced, which can directly impact the through-silicon-via technology, high density storage, photonic crystal membrane, and other related applications.

1. Introduction

Metal-assisted chemical etching (MacEtch or MaCE) is a robust and versatile process that has been adopted to overcome the limits of conventional semiconductor wet and dry etching technologies.[1–4] The advantage of producing high aspect ratio micro- and nano-structures with this simple and low-cost process has attracted attention for improving not only the etch quality but also the performance in many kinds of semiconductor device applications including light emitting diodes,[5] solar cells,[6–9] biosensors,[10] supercapacitors,[11] and thermoelectrics.[12]

The typical MacEtch process starts by patterning catalysts composed of noble metals (Au, Pt, Pd, Ag, Cu, Ni, etc.)[1,13–20] or graphene[21] on a semiconductor substrate or epitaxial structure. The catalyst layer can be patterned into any arbitrary geometry such as a mesh, dots, or trenches with micro- or nano-scale dimensions.[22] The substrate with metal patterns is then immersed in a chemical solution of an oxidant (e.g., hydrogen peroxide, H_2O_2) to oxidize and an acid (e.g., hydrofluoric acid, HF) to selectively etch the semiconductor localized under the patterned catalysts while the metal catalyst descends into the semiconductor.

MacEtch of silicon involves a pair of redox reactions: a cathodic reaction and an anodic reaction.[1] The cathodic reaction is the reduction reaction at the liquid/catalyst interface, which transfers the free electrons within the catalyst to the oxidant (H_2O_2). The anodic reaction is the half-reaction at the catalyst/silicon interface that produces the oxidized silicon by diffusing electrons from silicon to the catalyst, thus injecting holes. This oxidized region generated through hole-injection can then be selectively etched by HF.

The method of fabricating pillars or nanowires by MacEtch using interconnected mesh patterned catalyst layers has been well demonstrated, reaching aspect ratios as high as 200 for uniform nanowire arrays.[23–29] The process of fabricating high aspect ratio vias using MacEtch, which requires discrete dot catalyst patterns, is an important technique that can be applied to high density 2.5D/3D memory,[30] interconnects, through silicon vias (TSVs), photonic crystals, detectors, and many other

J. D. Kim, Prof. P. K. Mohseni, K. Balasundaram, Prof. X. Li
Department of Electrical and Computer Engineering
Micro and Nanotechnology Laboratory
Materials Research Laboratory
University of Illinois at Urbana–Champaign
IL 61801, USA
E-mail: xiuling@illinois.edu
Prof. X. Li
International Institute for Carbon-Neutral Energy Research (I2CNER)
Kyushu University
Fukuoka 819-0395, Japan
Prof. P. K. Mohseni
Microsystems Engineering
Rochester Institute of Technology
Rochester, NY 14623, USA
Dr. S. Ranganathan, Dr. J. Pachamuthu
SanDisk
a Western Digital Brand
Milpitas, CA 95035, USA
Prof. J. J. Coleman
Department of Electrical Engineering and Department of Materials Science
University of Texas at Dallas
Richardson, TX 75080, USA

DOI: 10.1002/adfm.201605614

© 2017 WILEY-VCH Verlag GmbH & Co. KGaA, Weinheim

technologies. Replacing the conventional reactive ion etching (RIE) process with MacEtch can minimize the unrepairable surface damages, including scallops and defects that can significantly degrade device performance.[30] Furthermore, MacEtch can accommodate the formation of high density via features with vertical sidewalls, whereas RIE is limited to the formation nanometer-scale features with tapered profiles. However, fabricating vias still remains a challenge due to the difficulty of minimizing the nonvertical catalyst motion resulting from the small, easily disturbed motion of the discrete metal catalysts that may result from nonuniform local carrier generation and mass transport. This phenomenon is henceforth referred to as detouring.

Previously, we reported a method for fabricating nanoscale vias on silicon-on-insulator wafers using the magnetic field-guided MacEtch (h-MacEtch).[31] In this study, trilayer catalysts of Au–Ni–Au were deposited, and externally applied magnetic fields were used to force the Ni perpendicular to the substrate to minimize catalyst detouring. Using this approach, vertical etch depths as function of the catalyst diameter from 900 to 400 nm at fixed pitch of 1 µm were determined. However, there are some challenges associated with using h-MacEtch to achieve high aspect ratio vias with nanoscale discrete catalysts. As the diameter decreases, the volume of the Ni is reduced. Thus, pull force from the magnetic field becomes too small to overcome nonvertical etching paths. Also, exposed Ni in trilayered catalysts gets etched by HF so that the etch time guided by the h-field is limited for small diameter catalysts.

One of the smallest via arrays fabricated with MacEtch was reported by Asoh et al.[32] They fabricated sub-100 nm silicon nanohole arrays using site-selective electroless deposition of Au and Ag on the anodic porous alumina on silicon substrate. They achieved an aspect ratio of 50 with 40 nm diameter and pitch of 100 nm. However, the uniformity of the diameter and pitch of the vias is affected by the anodic porous alumina, making it difficult to quantify the etch rate as a function of the catalyst dimension.

In MacEtch, the etch rate and etch profile are mainly governed by two mechanisms, carrier generation (CG) and mass transport (MT). The CG process involves the generation, injection, diffusion, and consumption of holes to oxidize the semiconductor, while the MT process involves the transport of reactants to, and byproducts away, from the etching front.[33,34] Both theoretical and experimental studies have been reported attempting to understand the mechanisms of CG and MT aspects in MacEtch in order to control etching rate, direction, and uniformity of the etching profile. Lianto et al. demonstrated the controlling of etching stability based on the excess hole concentration model by patterning arrays of stripes with varied catalyst dimensions and spacings in micron scale and MacEtching at varied H_2O_2 concentrations.[35] They observed that the hole concentration under a stripe overlaps with the one under the neighboring stripes that produces the curved trenches by enhancing the etch rate at catalyst edges (i.e., CG-limited process). Geyer et al. experimentally demonstrated the MT contribution by varying the catalyst thickness, and lateral dimension in continuous catalysts with microsized pore arrays and isolated nanostripe arrays.[34] Based on the etch rate decrease with increasing stripe width, they suggested that the transport of reactants and products under the metal influences the etch rate and profile. When MT was inhibited presumbaly by unsoluble oxide beneath the metal catalyst in the case of InP, only inverse-MacEtch took place.[36,37] Even more challenging but imperative for applications in modern electronics, one must understand and be able to control the CG and MT processes at the scale of 100 nm or less. So far, no clear understanding of the influence of MT and CG on the non-monolithic etch rate dependence on catalyst feature sizes has been shown, yet this is a step that has to be taken before ordered arrays of vias at this scale can be controllably produced.

In this work, we experimentally investigate the etch rate of sub-1 µm discrete catalyst dot arrays at fixed catalyst thickness, and with systematically varied diameter, pitch, and spacing as patterned by electron-beam lithography (EBL). By numerical data fitting, we extract the relationship between the measured etch rate and catalyst diameter, pitch, spacing, and concentration ratio of HF to H_2O_2. We find that the etch rate and profile of sub-1 µm discrete dot catalyst arrays can be suppressed or enhanced by manipulating the relative dominance of MT versus CG rate. We then demonstrate uniform and high density via arrays with dot features having diameters as small as 100 nm and separations as close as 80 nm.

2. Results and Discussion

Each sample contained patterns consisting of dot arrays of varied diameter from 100 to 900 nm at fixed pitch values of 1 µm for a diameter study, varied pitch from 300 to 900 nm at fixed diameter of 200 nm for a pitch study, and varied diameter from 100 to 600 nm at fixed spacing of 100 nm for a spacing study. Note that the diameter (D), pitch (P), and spacing (S) are defined as $S = P - D$. Samples were MacEtched in a solution containing a mixture of 49% HF, 30% H_2O_2, isopropyl alcohol (IPA), and deionized (DI) water. Here, we define the molar concentration ratio of H_2O_2 as

$$\rho_{H_2O_2} = \frac{H_2O_2[M]}{HF[M] + H_2O_2[M]} \tag{1}$$

$\rho_{H_2O_2}$ values of 0.19, 0.32, 0.41, and 0.48 were studied. **Figure 1** shows a set of paired top-view and 52° tilted-view focused ion beam (FIB) milled scanning electron microscope (SEM) images of via arrays with diameters stepping down from 600 to 100 nm in 100 nm increments at fixed spacing of 100 nm, produced by MacEtch in the solution of 0.41 $\rho_{H_2O_2}$ for 10 min. The via arrays show well-defined boundaries (top-view) and straight vertical profile (cross-section) for diameters down to 100 nm. Remarkably, the lateral detouring motion of the metal catalysts is effectively quenched under these etching conditions. Note that the narrowing of the vias with depth in the FIB cross-section is an artifact due to material redeposition during the ion milling.[38] The SEM images of other patterns with varied diameter at constant pitches, varied pitch at constant diameters, and varied diameter at constant spacing values, MacEtched at a series of concentrations ($\rho_{H_2O_2}$ = 0.19, 0.32, 0.41, and 0.48) can be found in the Supporting Information.

Figure 2a shows the measured vertical etch rate, as a function of the catalyst diameter with a constant pitch of 1 µm,

© 2017 WILEY-VCH Verlag GmbH & Co. KGaA, Weinheim

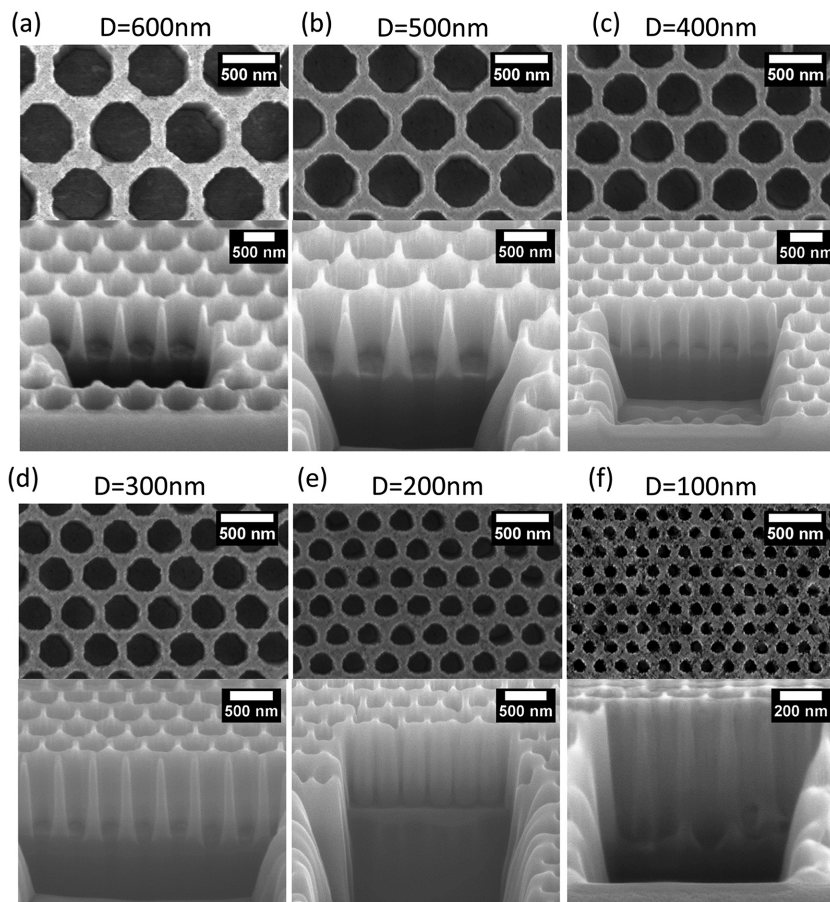

Figure 1. Pairs of top-view and FIB-milled 52° tilted-view SEM images of MacEtched via arrays in a solution of 0.56 M HF, 0.39 M H_2O_2, 0.88 M DI water, 0.21 M IPA for 10 min with via diameters of a) 600, b) 500, c) 400, d) 300, e) 200, and f) 100 nm, at a fixed spacing of 100 nm for all diameters.

MacEtched at $\rho_{H_2O_2}$ of 0.19, 0.32, 0.41, and 0.48. At 0.48 $\rho_{H_2O_2}$, the etch rate increases from 100 to 180 nm min^{-1} as the diameter increases from 100 to 500 nm; however, with continued increase of diameter, the etch rate starts to decrease to 130 nm min^{-1} at 900 nm (Figure 2a, blue curve). The red, green, and purple curves in Figure 2a represent etch results under identical conditions except $\rho_{H_2O_2}$ at 0.19, 0.32, and 0.41, respectively. The etch rate reduces with decreased H_2O_2 concentration due to reduced oxidation rates. A similar parabolic relationship between etch rate and diameter can be seen for etching under all of these conditions and, importantly, the diameter at the etch rate vertex (maximum etch rate), D_m, shows a clear shift to larger diameter with decreasing H_2O_2 concentration as indicated by the dashed trend line in Figure 2a. We attribute the parabolic trend of etch rate dependence on via diameter to the kinetic control of CG and MT in the MacEtch process. The MacEtch involves (1) CG to oxidize silicon, enabled by hole generation, hole diffusion, and hole injection, and (2) MT to remove the oxidized silicon, enabled by diffusion of reactants (HF, H_2O_2) to the reaction sites and products (H_2SiF_6, H_2O) away from the reaction sites. We denote the rate of these two critical steps as R_{CG} and R_{MT}. Note that R_{CG} lumps all steps related to electronic carriers and R_{MT} lumps all steps related to the transport of reactants and products. Because all of these subreactions take place in series, the slowest step determines the total etch rate, because $(R_{MacEtch})^{-1} = (R_{CG})^{-1} + (R_{MT})^{-1}$. When the diameter of the metal catalyst increases, the effective hole concentration (hole injection density × area) increases, while the oxidized material to be removed also increases. Higher CG rate corresponds to higher oxidation rate, while a larger diameter requires longer time for the oxidized silicon to be removed through lateral mass transport directly underneath the metal catalyst surface. As a result, the etch rate can be proportional or inversely proportional to catalyst diameter depending on which is the rate-determining step in the etching process. A CG rate-determined process should show an increase in etch rate with diameter (regimes to the left of the dashed trend line in Figure 2a), while the opposite is true for MT rate-determined process (regimes to the right of the dashed trend line). Thus, the etch condition under which the competition between CG and MT rates is balanced depends directly upon the diameter of the catalyst disk. An etch condition under which the CG and MT rates are comparable corresponds to the highest etch rate condition for the specific diameter, D_m.

Quantitatively, in the CG dominated regime in Figure 2a, the etch rate increases by a factor of ≈2 for the blue trace (0.48 $\rho_{H_2O_2}$) when the catalyst disk area increases by a factor of 25 (from 100 to 500 nm diameter). In the MT dominated regime for the same condition, the rate reduction from 600 to 900 nm diameter is only ≈20%, while the area increases by a factor of 3. In both regimes, the amount of rate increase or decrease is much less than the catalyst area change, indicating that the etch rate is limited by CG or MT, but with significant contribution from other mechanisms. Although the etch rate trend can be understood using the kinetics of the CG and MT processes, quantifying the rate dependence is not straightforward.

In addition to catalyst/via diameters, other etching conditions can affect the rate of CG and MT. Therefore, D_m can readily be shifted by tuning other experimental parameters, as shown in the four traces with varied H_2O_2 concentration in Figure 2a. When $\rho_{H_2O_2}$ decreases at a fixed HF concentration, the hole generation rate, thus oxidation rate, reduces, while the oxide dissolution rate remains the same, delaying the appearance of D_m.

Furthermore, the proximity between the vias can affect the etch rate significantly if carrier diffusion is allowed to play a role. This occurs when the CG rate is much higher than the MT rate, resulting in excess carriers not consumed for oxidation where they are generated. The carrier distribution profile under a metal catalyst disk can overlap with the ones under adjacent

© 2017 WILEY-VCH Verlag GmbH & Co. KGaA, Weinheim

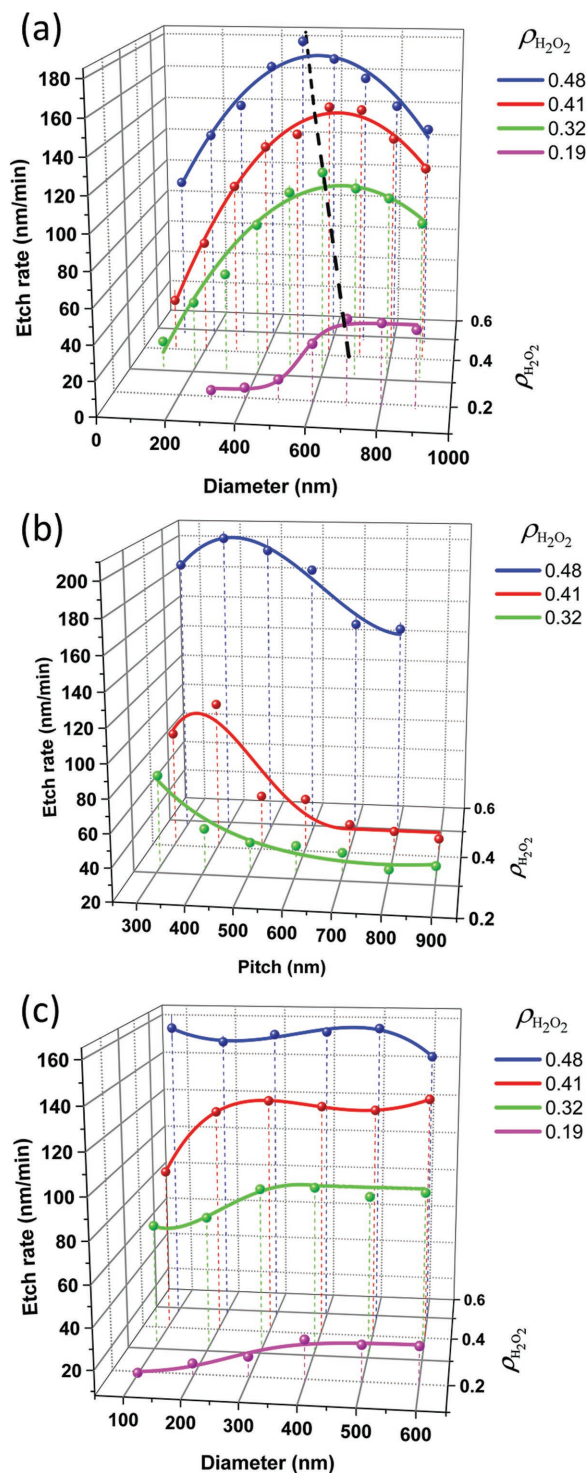

Figure 2. Vertical etch rate plotted as a function of a) diameter (D) at a fixed pitch (P) of 1 µm, b) pitch (P) at a fixed diameter of 200 nm, and c) diameter (D) at fixed spacing of 100 nm, MacEtched at $\rho_{H_2O_2}$ of 0.19, 0.32, 0.41, and 0.48. The symbols represent measured etch rates averaged over six data points at each condition, connected by the solid fitting lines. The dashed line in (a) indicates the trend for peak etch rate (vertex of the paraboloid).

catalyst pads and produce enhanced oxidation locally. Figure 2b shows the etch rate as a function of the catalyst pitch from 300 to 900 nm at a constant diameter of 200 nm, MacEtched at $\rho_{H_2O_2}$ of 0.32, 0.41, and 0.48 as indicated. We first examine the trend as the pitch reduces; i.e., the vias become more and more closely spaced. In the pitch range studied here, for the two lower $\rho_{H_2O_2}$ cases, the etch rate maintains a near constant value almost independent of pitch at the large pitch end. As the pitch decreases, the etch rate starts to increase for all cases, but with different threshold (P_{th}) for the upward slope for different $\rho_{H_2O_2}$. For the two high $\rho_{H_2O_2}$ cases, further reduction of the pitch between the catalyst pads (from 400 to 300 nm) results in a decrease of etch rate.

We attribute the enhanced etch rate with closer spacing to the overlap of hole concentration profiles between neighboring catalysts as a result of carrier diffusion. This can only occur when there is an excess of holes in the process; i.e., the generated holes at the catalyst surface do not get consumed at the catalyst/silicon interface to oxidize silicon oxidation immediately. Such hole concentration overlap increases the depth of the oxidized silicon similar to the influence of increased H_2O_2 concentration, but at a local level. This enhancement can be a result of synergized catalytic effect or simply physical overlap of the carrier distribution profiles under each catalyst disk. The fact that porosity is enhanced between the vias (see SEM in Figure S6 in the Supporting Information) supports the latter. The porosity observed here does not affect the local vertical etch rate normal to the catalyst surface, since the rate-determine step in these cases is mass transport and has little to do with how much excess carriers are generated or migrated to generate porous Si. Porosity formation did not cause detouring of the catalyst either in these cases, but it can happen under a strongly MT-limited case with extremely high oxidant concentration that leads to nonuniform hole concentration profiles under the catalyst. Naturally, the lower the H_2O_2 concentration in solution, the smaller the pitch needs to be before hole concentration overlaps and induces etch rate enhancement. This is in complete agreement with observations in Figure 2b, where the minimum pitch that corresponds to etch rate rise threshold (P_{th}) is ≈400, 600, >800 nm for $\rho_{H_2O_2}$ of 0.32, 0.41, and 0.48, respectively. At the same time, the decrease of catalyst spacing eventually causes a shortage of HF required to remove the increased oxidized silicon per unit area and the reaction becomes MT-limited. The decrease in total etch rate at pitch values below 400 nm for 0.41 and 0.48 $\rho_{H_2O_2}$ indicates that the reduction in etch rate attributed to the MT-limited process is larger than the etch rate enhancement contribution from the hole concentration overlap. Note that despite the increased excess hole concentration, catalyst deformation was not observed as previously reported in micron-scale stripe MacEtch.[35] This can be explained by the enhanced MT from reduced catalyst dimension,[34] and the appropriate oxidization to dissolution ratio.

To separate the effect of catalyst diameters and proximity effect between adjacent catalysts, Figure 2c shows the vertical etch rate as a function of catalyst diameter at a fixed catalyst spacing of 100 nm, MacEtched at $\rho_{H_2O_2}$ of 0.19, 0.32, 0.41, and 0.48. We chose a close spacing of 100 nm to emulate a more demanding potential device architecture. For $\rho_{H_2O_2}$ of 0.19, the etch rate decreases from ≈30 to ≈10 nm min^{-1} as the diameter decreases from 400 to 100 nm due to the CG-limited process. The diameter where the etch rate decreases shifts to 300 and 200 nm as the $\rho_{H_2O_2}$ increases to 0.32 and 0.41, respectively. We

© 2017 WILEY-VCH Verlag GmbH & Co. KGaA, Weinheim

attribute this to the increased hole concentration, as described in the case of the diameter study at fixed pitch (Figure 2a). It can be seen that the etch rate above the diameter of 400, 300, and 200 nm for $\rho_{H_2O_2}$ of 0.19, 0.32, and 0.41, respectively, is saturated. For the 0.48 $\rho_{H_2O_2}$ case, the etch rate over the entire diameter range studied is nearly constant. These observations imply that once the hole concentration is above a threshold level, the parabolic trend etch rate dependence with diameter can be defied. When the diameter increases, the etch rate is increased by enhanced CG. However, the etch rate is simultaneously decreased by the reduced MT due to increased packing density. We attribute the weak dependence of etch rate on via diameter when they are closely spaced (100 nm) to the near perfect balance between R_{CG} increase (due to increased hole injection with increasing diameter and carrier profile overlap) and R_{MT} decrease (due to the reduced etchant and byproduct transport with increasing diameter and depleted etchant resulted from the increased catalyst packing density). Note that depending on the catalyst pattern, R_{CG} and R_{MT} may reach steady state, as reported previously in the work of Yeom et al. on MacEtch of Si nanowire arrays.[39]

To provide further understanding of the etching mechanism, next we extract an etch rate model based on the experimental data and examine the physical meaning of the parameters. The empirical model is constructed by fitting the etch rate data as a function of diameter at fixed pitch of 1 µm shown in Figure 2a using a second order polynomial, in the form of Equation (2)

$$R_{\text{Vertical}} = a + b(P - D) - c(P - D)^2 \quad (2)$$

where R_{Vertical} is the vertical MacEtch rate in nm min^{-1}, D, P are the diameter and the pitch of catalyst pads in µm, a is the intercept, b and c are the first and second order polynomial coefficients. The best fitting results for coefficients a, b, and c with $\rho_{H_2O_2}$ as the variable can be found in the Supporting Information. By expanding the quadratic term and regrouping D and P terms, Equation (2) becomes

$$R_{\text{Vertical}} = a + \left(bP - cP^2 + 2cDP\right) + \left(-bD - cD^2\right) \quad (3)$$

By assigning $\delta R_{MT} = -bD - cD^2$ (vertical etch rate decreased by limited MT, related to D only) and $\delta R_{CG} = bP - cP^2 + 2cDP$ (vertical etch rate increased under CG-limited condition, related to D and P)

$$R_{\text{Vertical}} = a + \delta R_{MT} + \delta R_{CG} \quad (4)$$

It is important to note that the processes of MT and CG are in series in nature. The expression in Equation (4), although in summation form, δR_{MT} and δR_{CG} are not parallel or independent of each other, because they share the same variables of b, c, and D. The physical meaning of each term in this rate model can be validated by analyzing the relationship between R_{Vertical} and D, P at low and high ends of $\rho_{H_2O_2}$. The calculated a, b, c, and R_{Vertical} values, as well as δR_{MT} and δR_{CG} terms by plugging $\rho_{H_2O_2} = 0.1$ and 0.9, are listed in **Table 1**. Here, the a coefficient corresponds to the etch rate when $D = 0$ (i.e., without any catalyst); thus, a should be close zero, but increases with $\rho_{H_2O_2}$. Setting $P = 1$ µm, we have $\delta R_{MT} = -bD - cD^2$ and $\delta R_{CG} = b - c + 2cD$. At $\rho_{H_2O_2} = 0.1$, b is much smaller than c (see Table 1) such that R_{Vertical} is dominated by the $2cD$ term in δR_{CG} (note that $D < 1$ so D^2 term is smaller than D term); i.e., R_{Vertical} is dominated by δR_{CG}, which is linearly proportional to D to first order approximation. At $\rho_{H_2O_2} = 0.9$, the linear term almost cancels out and the total rate is dominated by the D^2 term in δR_{MT}.

Table 1. Etch rate model parameters and relationships at high and low ends of $\rho_{H_2O_2}$.

$\rho_{H_2O_2}$	a	b	c	$P = 1$ µm ($D < 1$)		
				δR_{MT}	δR_{CG}	R_{Vertical}
0.1	11.2	19.5	320.7	$-19.5D - 320.7D^2$	$-301.2 + 641.4D$	$\approx\delta R_{CG} \propto D$
0.9	54.5	589.5	320.9	$-589.5D - 320.9D^2$	$286.6 + 641.8D$	$\approx\delta R_{MT} \propto -D^2$

Using this empirical model, the etch rate as a function of diameter at a fixed pitch, and diameter at a fixed spacing are simulated for the entire range of H_2O_2 from 0.1 to 0.9 with 0.1 step, as shown in **Figure 3**a–c.

Figure 3a shows the dependence of etch rate at $P = 1$ µm on diameters, including beyond the experimentally explored range of H_2O_2. At low $\rho_{H_2O_2}$ of 0.1 and 0.2, the etch rate is near zero until D increases beyond a threshold value, presumably when sufficient amount of carriers are generated to initiate the surface oxidation. At high $\rho_{H_2O_2}$ of 0.9, where the etch rate decreases monotonically with increasing D, indicating that the etch rate at this high $\rho_{H_2O_2}$ concentration is completely limited by MT (δR_{MT}). Other than the extreme low and high ends of $\rho_{H_2O_2}$, the parabolic dependence persists throughout most of the $\rho_{H_2O_2}$ range. The decrease of D_m (the diameter at maximum etch rate) with increasing $\rho_{H_2O_2}$ indicates that the onset of total vertical etching shifts with a critical hole concentration that is controlled by a combination of both the catalyst diameter and oxidant concentration.

Figure 3b shows the simulated etch rate as a function of pitch at a fixed diameter of 200 nm, for the entire $\rho_{H_2O_2}$ range from 0.1 to 0.9. Similar to the low $\rho_{H_2O_2}$ case in Figure 2c, the simulated trend lines reveal that at low $\rho_{H_2O_2}$ (0.1 and 0.2), there is a threshold pitch (P_{th}), below which the etch rate starts to increase. P_{th} increases from 300 to 800 nm as increases from 0.1 to 0.2. At intermediate $\rho_{H_2O_2}$ range (0.2–0.7), the parabolic etch rate trend resulting from CG and MT imbalance starts to appear and the vertex; i.e., the pitch corresponding to the highest etch rate pitch, P_m, increases as $\rho_{H_2O_2}$ increases. This is in complete agreement with the hypothesis of increased CG rate due to carrier concentration profile overlap between adjacent catalyst features. The proximity of the catalyst features causes an overlap of adjacent carrier hole profiles, which occurs at larger pitch values when $\rho_{H_2O_2}$ increases. At high $\rho_{H_2O_2}$, the etch rate monotonically increases with pitch, indicating that the etch rate is completely dominated by the MT process. Note that since the model was extracted based on the experimental data set at large D and a constant pitch of 1 µm (Figure 2a), the simulated values of etch rate and $\rho_{H_2O_2}$ are overestimated and should not be taken literally, but the trends shown are clearly validated by the kinetics of CG and MT.

Figure 3c shows the simulated etch rate as a function of diameter at a fixed spacing of 100 nm. A constant etch rate

© 2017 WILEY-VCH Verlag GmbH & Co. KGaA, Weinheim

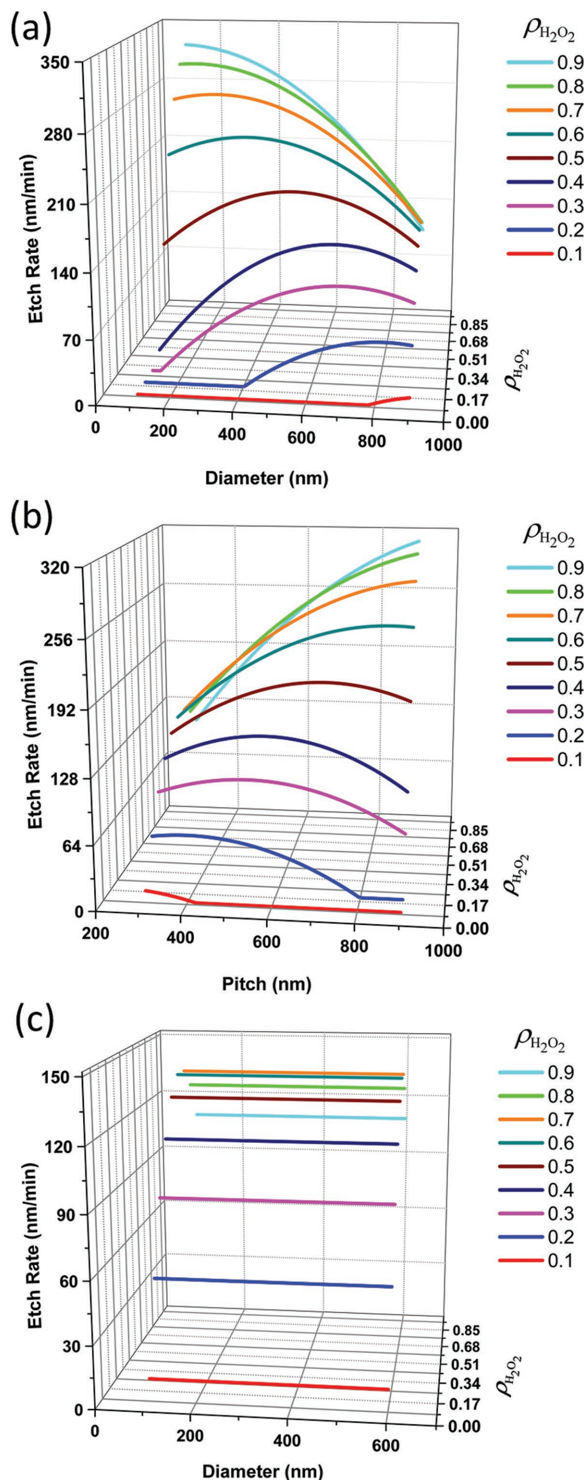

Figure 3. Simulated vertical etch rate as a function of a) diameter at 1 μm fixed pitch, b) pitch at 200 nm diameter, c) diameter at 100 nm fixed spacing with varied $\rho_{H_2O_2}$ from 0.1 to 0.9.

over the entire diameter range can be seen for all concentrations simulated. Compared to the experimental result shown Figure 2c, the simulated data do not show the decrease in etch rate at small diameter for low $\rho_{H_2O_2}$, because the threshold hole concentration required at equal spacing is not included in the empirical model. Nonetheless, the etch rate independent of diameter over a broad range of $\rho_{H_2O_2}$ shown here validates the hypothesis where the close proximity related carrier concentration profile overlap helps balance the CG and MT processes to reach steady state.

The steady state etch rate gradually increases as $\rho_{H_2O_2}$ increases and saturates when $\rho_{H_2O_2}$ reaches 0.7, then starts to decrease as $\rho_{H_2O_2}$ increases from 0.7 to 0.9. The saturation of etch rate as $\rho_{H_2O_2}$ continues to increase (<0.7) is the result of the transition from CG-limited to MT-limited kinetic process, where the etch rate is governed by MT or HF concentration, invariant with regard to $\rho_{H_2O_2}$. The etch rate did not remain saturated with further increased H_2O_2 (>0.7) and this is attributed to a second order effect specific to the etching condition, where HF, IPA, DI water volumes were kept constant while H_2O_2 continues to increase. When HF is diluted by the addition of increasing volume of H_2O_2, the oxide removal rate starts to decrease, breaking down the independence to $\rho_{H_2O_2}$ even though the oxidation rate is saturated. Under the reported etch condition, the breakdown of the etch rate plateau occurs at $\rho_{H_2O_2}$ of 0.7 and continues to decrease thereafter.

The systematic analysis of the etching kinetics as a function of catalyst diameter, pitch, spacing, and etchant concentration presented above provides guidance on producing vias under the highest etch rate not only for high efficiency but also to minimize catalyst detouring and porosity around the vias, and ensure vertical etch profiles.

It is worth noting that MacEtch uniformity and reproducibility are also remarkably sensitive to residual poly methyl methacrylate (PMMA) from the EBL process. Some examples of unsuccessful vertical via-MacEtch cases as a result of PMMA under- or over- exposure and development either globally or locally, easily led to the detouring of the catalyst disks, as can be clearly seen in Figure S14 (Supporting Information). Detailed analysis of the detouring direction and trajectory can also be found in the Supporting Information. Only by methodically optimizing electron beam dosage, PMMA developing time, and residue cleaning process, the adverse influence of the undesired resist layer can be mitigated. Uniform MacEtch can be realized only when the interface between the Au catalyst and substrate is free of PMMA residue in both large and small diameter patterns. This is of paramount importance for MacEtch, particularly for vertical progression of an etch-front when using discrete catalyst.

By overcoming the EBL related interface issues and with precise control of the etch rate, uniform and vertical vias can be achieved by MacEtch. **Figure 4**a shows a cross-sectional SEM image, obtained by mechanical cleaving through the etched vias, where a perfectly vertical etch profile can be seen for a MacEtched sample with catalyst diameters of 320 nm and spacing of ≈80 nm. An etching depth of >3 μm is realized, generating closely spaced nanoscale Si vias of aspect ratio >10 within a 10 min MacEtch procedure. Figure 4b,c shows low and high magnification top-view SEM images of the via array, respectively. Figure 4d shows cross-sectional SEM image of the Au catalysts at the bottom of the etched vias.

In addition to producing single crystal high aspect ratio vertical vias, we have achieved the same for polycrystalline silicon,

© 2017 WILEY-VCH Verlag GmbH & Co. KGaA, Weinheim

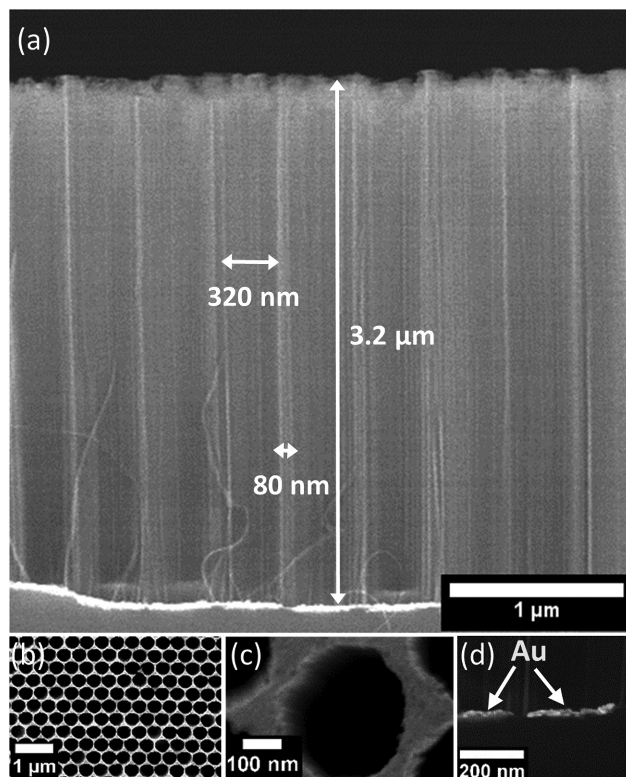

Figure 4. a) Cross-sectional SEM image, obtained by direct mechanical cleaving to reveal the sidewalls of the MacEtched sample with 320 nm diameter and 400 nm pitch (i.e., 80 nm spacing) dot catalyst array. A vertical etching depth of 3.2 µm is observed. b) Low magnification top-view SEM image of via array. c) High magnification top-view SEM image of via. d) The Au catalyst disks can be clearly seen at the bottom of the etched vias.

where the catalyst detouring is significantly more severe. The MacEtch condition that produced ordered vertical via arrays for single crystal silicon only yielded disordered morphologies, revealing massively detoured catalyst trajectories in polycrystal etching, presumably due to the nonuniform multicrystal orientation etch rate across the metal catalyst pads. Rebalancing the CG and MT rates in the process was necessary through catalyst engineering to ensure vertical descent of the catalysts into the body of polycrystalline silicon, and the results will be reported separately.

3. Conclusion

In conclusion, we have demonstrated the influence of MT and CG on vertical MacEtch rate of isolated catalyst arrays by systematically varying catalyst disk diameter, pitch, and spacing in submicron dimensions. Under constant pitch values, a transition from an increasing etch rate to a decreasing etch rate shows that the dominance of the MT or CG can be manipulated by controlling the catalyst diameter. A maximum vertical etch rate is found at a critical diameter, which can be shifted with varying H_2O_2 concentration. This indicates that MT and CG can either be enhanced or suppressed by varying the oxidant concentration ratio or metal catalyst diameter. Variations in etch rate as a function of catalyst pitch under fixed diameters show a notable enhancement with decreasing pitch, which has been attributed to an overlap of neighboring injected hole concentration profiles. However, this enhancement is also limited by the same solution volume being shared by a larger oxidized volume resulting from a higher catalyst packing density. Analysis of etch rates as a function of catalyst diameter at fixed spacing shows that CG in the small diameter regime is enhanced by increasing H_2O_2 concentration, but etch rates in the large diameter regime are compensated by limited MT that results from limited solution access. The mechanism study of the influence of the MT and CG in MacEtch of isolated catalyst arrays provides a detailed understanding of etch rate manipulation and etch direction control. Insights gained from this study not only should help achieve high aspect ratio and closely spaced submicron size vias required for high areal density memory and optoelectronic devices, but also large and sparsely spaced hole arrays for other applications including TSV interconnect for 3D integrated circuits.

4. Experimental Section

Boron doped p-type (100)-oriented single crystalline Si substrates with resistivity of 1–20 Ω cm were used for all experiments. The Si substrate was first subjected to a cleaning process for organic contaminant removal in 1:1:5 ammonium hydroxide (NH_4OH):H_2O_2:DI water at 80 °C, followed by native oxide strip in 1:10 buffer oxide etchant (BOE), and ionic contaminant removal in 1:1 hydrogen chloride (HCl):DI water. After the sample was dried with N_2, electron beam resist of 950 PMMA in 2% anisole was spin-coated at 2500 rpm for 30 s (800 nm thickness) and baked at 200 °C for 2 min. Then, EBL was carried out at 10 kV beam voltage, through a 20 µm aperture, with areal exposure mode for exposure of the specified dot array patterns. The diameter of the patterns was first coarse-tuned with areal dose of 100 µC cm^{-2}, and fine-tuned with local electron beam dosage. After exposure, patterns were developed in 1:3 methyl isobutyl keton:IPA for 2 min at room temperature. Then, 10 nm Au was deposited by electron-beam evaporation after PMMA residues, native oxide, and ionic contamination on the exposed patterns were etched with 1:10 BOE for 2 min, and 1:1 HCl:DI water for 1 min. After the deposition, the Au film was lifted off in Remover PG (MicroChem Corp.) for 30 min at 60 °C. Samples with hexagonally symmetric Au catalyst arrays were MacEtched in a solution of 49% HF (0.56 M), 30% H_2O_2 (0.13, 0.26, 0.39, 0.52), IPA (0.21 M), and DI water (0.88 M), and inspected with a Hitachi S-4800 SEM. Sample milling for cross-sectional imaging was performed using an FEI DB235 dual-beam FIB system; low Ga+ ion currents (≈10 pA) were used at 30 kV accelerating voltage for sample damage mitigation. A regular cross-section milling pattern was first used to mill down to the bottom of the Au catalyst, then a cleaning cross-section milling pattern was used to mill the redeposited debris resulting from the initial milling step.

Supporting Information

Supporting Information is available from the Wiley Online Library or from the author.

Acknowledgements

This work was supported in part by the National Science Foundation through the Civil, Mechanical and Manufacturing Innovation

© 2017 WILEY-VCH Verlag GmbH & Co. KGaA, Weinheim

under Grant 14-62946, a gift from Western Digital Corporation, and I2CNER.

Received: October 26, 2016
Revised: December 17, 2016
Published online:

[1] X. Li, P. W. Bohn, *Appl. Phys. Lett.* **2000**, *77*, 2572.
[2] X. Li, *Curr. Opin. Solid State Mater. Sci.* **2012**, *16*, 71.
[3] Z. Huang, N. Geyer, P. Werner, J. de Boor, U. Gösele, *Adv. Mater.* **2011**, *23*, 285.
[4] H. Han, Z. Huang, W. Lee, *Nano Today* **2014**, *9*, 271.
[5] P. K. Mohseni, S. H. Kim, X. Zhao, K. Balasundaram, J. D. Kim, L. Pan, J. A. Rogers, J. J. Coleman, X. Li, *J. Appl. Phys.* **2013**, *114*, 064909.
[6] K.-Q. Peng, X. Wang, L. Li, X.-L. Wu, S.-T. Lee, *J. Am. Chem. Soc.* **2010**, *132*, 6872.
[7] W. Chern, K. Hsu, I. S. Chun, B. P. de Azeredo, N. Ahmed, K.-H. Kim, J.-M. Zuo, N. Fang, P. Ferreira, X. Li, *Nano Lett.* **2010**, *10*, 1582.
[8] H. Um, N. Kim, K. Lee, I. Hwang, J. H. Seo, Y. J. Yu, P. Duane, M. Wober, K. Seo, *Sci. Rep.* **2015**, *5*, 11277.
[9] W. Jevasuwan, K. Nakajima, Y. Sugimoto, N. Fukata, *Jpn. J. Appl. Phys.* **2016**, *55*, 065001.
[10] M. K. Dawood, L. Zhou, H. Zheng, H. Cheng, G. Wan, R. Rajagopalan, H. P. Too, W. K. Choi, *Lab Chip* **2012**, *12*, 5016.
[11] S.-W. Chang, J. Oh, S. T. Boles, C. V. Thompson, *Appl. Phys. Lett.* **2010**, *96*, 153108.
[12] A. I. Hochbaum, R. Chen, R. D. Delgado, W. Liang, E. C. Garnett, M. Najarian, A. Majumdar, P. Yang, *Nature* **2008**, *451*, 163.
[13] H. Asoh, F. Arai, S. Ono, *Electrochim. Acta* **2009**, *54*, 5142.
[14] K. Q. Peng, J. J. Hu, Y. J. Yan, Y. Wu, H. Fang, Y. Xu, S. T. Lee, J. Zhu, *Adv. Funct. Mater.* **2006**, *16*, 387.
[15] A. Hidetaka, A. Fusao, U. Kota, O. Sachiko, *Appl. Phys. Express* **2008**, *1*, 067003.
[16] J.-P. Lee, S. Choi, S. Park, *Langmuir* **2011**, *27*, 809.
[17] V. Kapaklis, A. Georgiopoulos, P. Poulopoulos, C. Politis, *Phys. E* **2007**, *38*, 44.
[18] S. Chattopadhyay, P. W. Bohn, *Anal. Chem.* **2006**, *78*, 6058.
[19] R. A. Lai, T. M. Hymel, V. K. Narasimhan, Y. Cui, *ACS Appl. Mater. Interfaces* **2016**, *8*, 8875.
[20] O. J. Hildreth, D. R. Schmidt, *Adv. Funct. Mater.* **2014**, *24*, 3827.
[21] J. Kim, D. H. Lee, J. H. Kim, S.-H. Choi, *ACS Appl. Mater. Interfaces* **2015**, *7*, 24242.
[22] H. Hu, P. K. Mohseni, L. Pan, X. Li, S. Somnath, J. R. Felts, M. A. Shannon, W. P. King, *J. Vac. Sci. Technol., B* **2013**, *31*, 06FJ01.
[23] B. P. Azeredo, J. Sadhu, J. Ma, K. Jacobs, J. Kim, K. Lee, J. H. Eraker, X. Li, S. Sinha, N. Fang, P. Ferreira, K. Hsu, *Nanotechnology* **2013**, *24*, 225305.
[24] J. C. Shin, D. Chanda, W. Chern, K. J. Yu, J. A. Rogers, X. Li, *IEEE J. Photovolt.* **2012**, *2*, 129.
[25] J. C. Shin, C. Zhang, X. Li, *Nanotechnology* **2012**, *23*, 305305.
[26] K. Balasundaram, J. S. Sadhu, J. C. Shin, B. Azeredo, D. Chanda, M. Malik, K. Hsu, J. A. Rogers, P. Ferreira, S. Sinha, X. Li, *Nanotechnology* **2012**, *23*, 305304.
[27] J. Kim, Y. H. Kim, S.-H. Choi, W. Lee, *ACS Nano* **2011**, *5*, 5242.
[28] S. Li, W. Ma, Y. Zhou, X. Chen, Y. Xiao, M. Ma, W. Zhu, F. Wei, *Nanoscale Res. Lett.* **2014**, *9*, 1.
[29] Y. Qi, Z. Wang, M. Zhang, F. Yang, X. Wang, *J. Phys. Chem. B* **2013**, *117*, 25090.
[30] X. Zhang, J. K. Lin, S. Wickramanayaka, S. Zhang, R. Weerasekera, R. Dutta, K. F. Chang, K.-J. Chui, H. Y. Li, D. S. Wee Ho, L. Ding, G. Katti, S. Bhattacharya, D.-L. Kwong, *Appl. Phys. Rev.* **2015**, *2*, 021308.
[31] K. Balasundaram, P. K. Mohseni, Y.-C. Shuai, D. Zhao, W. Zhou, X. Li, *Appl. Phys. Lett.* **2013**, *103*, 214103.
[32] H. Asoh, K. Fujihara, S. Ono, *Nanoscale Res. Lett.* **2013**, *8*, 410.
[33] L. Li, Y. Liu, X. Zhao, Z. Lin, C.-P. Wong, *ACS Appl. Mater. Interfaces* **2014**, *6*, 575.
[34] N. Geyer, B. Fuhrmann, Z. Huang, J. de Boor, H. S. Leipner, P. Werner, *J. Phys. Chem. C* **2012**, *116*, 13446.
[35] P. Lianto, S. Yu, J. Wu, C. V. Thompson, W. K. Choi, *Nanoscale* **2012**, *4*, 7532.
[36] S. H. Kim, P. K. Mohseni, Y. Song, T. Ishihara, X. Li, *Nano Lett.* **2015**, *15*, 641.
[37] Y. Song, P. K. Mohseni, S. H. Kim, J. C. Shin, T. Ishihara, I. Adesida, X. Li, *IEEE Electron Device Lett.* **2016**, *37*, 970.
[38] Y. Q. Fu, N. K. A. Bryan, O. N. Shing, N. P. Hung, *Int. J. Adv. Manuf. Technol.* **2000**, *16*, 877.
[39] J. Yeom, D. Ratchford, C. R. Field, T. H. Brintlinger, P. E. Pehrsson, *Adv. Funct. Mater.* **2014**, *24*, 106.

© 2017 WILEY-VCH Verlag GmbH & Co. KGaA, Weinheim